Journal of Computing and Electronic Information Management
ISSN: 2413-1660 | Vol. 20, No. 3, 2026

Research on Physically-Constrained Continuous-Time Dynamical Models and Precise Smartphone Battery Life Prediction

Zhipeng Zhang*

School of Science, Shandong Jianzhu University, Jinan, 250000, China
***Corresponding author Email:** eltg567@gmail.com

Abstract: Addressing the challenge of balancing prediction accuracy and interpretability in smartphone battery life forecasting, this study constructs a physically-driven continuous-time dynamical model and a dynamically calibrated Time-to-End-of-Life (TTE) prediction system. The study first decomposes battery output power into external loads and internal losses based on the law of energy conservation, coupling it with a first-order lumped-parameter thermal model. To address user behavior randomness, a continuous-time Markov chain simulation mode switching is introduced, utilizing an Unscented Kalman Filter (UKF) for online parameter calibration. Empirical results demonstrate that this model accurately describes the evolution trajectory of the state of charge (SOC) under various load and temperature conditions. Specifically, the framework achieves precise runtime estimation across diverse scenarios—predicting TTE from 10.69 hours in compute-heavy modes to 23.46 hours in light-load modes—and identifies CPU operations as the primary energy consumption driver, while revealing GPS impact is negligible. This study provides a systematic quantitative solution for energy efficiency management and high-precision runtime prediction in mobile devices.

Keywords: Continuous-time model; Remaining runtime prediction; Unscented Kalman filter.

1. Introduction

With the proliferation of mobile internet, smartphones have become central tools in modern life. However, the runtime performance of their lithium-ion batteries exhibits significant complexity and dynamism, influenced by multiple intertwined factors including user behavior, ambient temperature, and aging. Achieving high-precision State-of-Charge (SOC) tracking and Time-to-Discharge (TTE) prediction with limited sensor data has become a critical challenge for optimizing user experience and system energy efficiency management. Previous studies have primarily focused on simple statistical regression or black-box discretization models, which, while offering reasonable accuracy in specific scenarios, often lack physical interpretability and struggle to effectively address prediction uncertainties caused by sudden load fluctuations and environmental temperature disturbances. This section innovates by proposing a physically constrained continuous-time modeling framework. Through non-negative power decomposition and a fast-slow hierarchical estimation mechanism, it achieves deep integration between physical mechanism modeling and stochastic behavior modeling. A dynamic calibration algorithm is introduced to eliminate parameter drift. The overall research approach follows rigorous mathematical logic: First, we establish the master equations of battery dynamics encompassing multi-module power consumption, thermal coupling, and health evolution [1]. Subsequently, we develop a TTE probabilistic prediction algorithm based on mode switching and state space reconstruction. Finally, through multi-scenario simulation validation and error decomposition, we quantify the contribution weights of each hardware module to endurance and assess the models robustness under various uncertainty sources. Empirical results demonstrate that the model accurately tracks the evolution trajectory of state of charge (SOC) under diverse load and temperature conditions, with prediction points uniformly distributed along the ideal 45° line in validation tests. Specifically, the model precisely quantifies runtime across distinct scenarios, predicting TTE from 10.69 hours in compute-heavy modes to 23.46 hours in light-load modes. Furthermore, attribution analysis identifies CPU operations as the primary energy consumption driver, while revealing that GPS usage has a negligible impact on battery drain within the tested data range.

2. Model Establishment

2.1. Model I: Continuous-Time Battery Dynamics Model

2.1.1. Modeling Motivation and Overall Framework

The difference in smartphone battery life speed is not caused by a single factor, but by the combined effect of external load power consumption and the internal state of the battery. The battery discharge process is constrained by the law of conservation of energy. The effective available energy of lithium-ion batteries changes significantly with temperature and health status. Long-term charging and discharging history of the battery will also lead to capacity degradation and internal resistance increase, making the rate of state of charge (SOC) decline faster under the same load. Therefore, the modeling goal of this study is to construct a continuous-time SOC dynamic model, which should be able to output the dynamic change curve of SOC, explain the influence path of various driving factors on battery power consumption, and provide a computable model foundation for subsequent remaining usage time prediction and uncertainty analysis [2-3].

The mind map of the model is as figure 1:

Figure 1. Mind map of the continuous-time battery dynamics model

2.1.2. Output Power Decomposition and Physical Constraints

To accurately characterize the distribution mechanism of battery output power and correspond to the aforementioned analysis framework of multi-power supply scenarios, we divide the battery output power into two parts: external load power consumption $P_{load}(t)$ and internal loss power $P_{loss}(t)$. The equivalent output power at the battery terminal is:

$$P_{batt}(t) = P_{load}(t) + P_{loss}(t) \quad (1)$$

Among them, the external load power consumption represents the power supplied by the battery for user behavior and system operation, and the internal loss power corresponds to irreversible energy losses such as self-heating and internal resistance of the battery. Both satisfy non-negativity constraints $P_{load}(t) \geq 0$ and $P_{loss}(t) \geq 0$ to conform to physical reality [4-6].

To further clarify the driving sources of battery life attenuation, we decompose the external load power consumption into the sum of basic noise and power consumption of each functional module for interpretability according to hardware and system modules:

$$P_{load}(t) = P_0 + P_s(t) + P_c(t) + P_n(t) + P_g(t) + P_a(t) \quad (2)$$

Where $P_0 \geq 0$ represents the system standby noise; P_s, P_c, P_n, P_g, P_a correspond to the power consumption of the screen, CPU, network, GPS, and background tasks respectively. This structure enables the model to answer questions required by the problem such as "which activities lead to the most significant reduction in battery life and which have little impact".

To ensure interpretability and avoid the risk of "pure regression being divorced from physics", we express each power consumption item as a non-negative mapping of observable features:

$$P_s(t) = \alpha_s f_s(b(t)),\ P_c(t) = \alpha_c f_c(c(t)),\ P_n(t) = \alpha_n f_n(n(t)),\ P_g(t) = \alpha_g f_g(g(t)),\ P_a(t) = \alpha_a f_a(a(t)) \quad (3)$$

Where $f_*(\cdot)$ can be linear or piecewise linear, and constraints such as $\alpha_* \geq 0$ and $P_0 \geq 0$ are imposed to ensure that the power consumption components do not appear non-physical negative values [7].

2.1.3. SOC Master Equation and Thermal Coupling Equation

(1) Derivation of the SOC Master Equation

Let $E(t)$ be the remaining available energy of the battery at time t, and define the effective maximum energy as $E_{max}(T, H) > 0$, which changes with temperature and health. Then:

$$SOC(t) = \frac{E(t)}{E_{max}(T(t), H(t))} \quad (4)$$

According to the law of conservation of energy, the decay rate of battery energy storage is equal to the negative value of its external output power:

$$\frac{dE(t)}{dt} = -P_{batt}(t) \quad (5)$$

Taking the total differential of the definition of remaining available energy and combining it with the energy conservation equation, we obtain:

$$\frac{dE}{dt} = E_{max}\frac{dSOC}{dt} + SOC\frac{\partial E_{max}}{\partial T}\frac{dT}{dt} + SOC\frac{\partial E_{max}}{\partial H}\frac{dH}{dt} = -P_{batt}(t) \quad (6)$$

On the time scale of daily discharge, the changes in battery temperature and health status are relatively slow. Therefore, the slow-varying terms related to T and H in the equation can be simplified through a slow-layer update process or noise absorption, and finally the continuous-time SOC master equation is obtained:

$$\frac{dSOC}{dt} = -\frac{P_{batt}(t)}{E_{max}(T(t), H(t))},\ 0 \leq SOC(t) \leq 1 \quad (7)$$

This equation clearly reflects the physical mechanism: the greater the external load power, or the smaller the effective maximum energy of the battery due to low temperature and aging, the faster the SOC decline rate[8-9].

(2) Internal Loss Term

Ohmic loss and polarization loss inside the battery will consume additional energy. To characterize this effect and retain the mechanism exit of "operating load, temperature rise, and battery aging", this study adopts an equivalent loss ratio form:

$$P_{loss}(t) = \kappa(T(t), H(t))\ P_{load}(t),\ \kappa(T, H) \geq 0 \quad (8)$$

This form not only intuitively reflects the law that "the greater the load, the greater the loss", but also allows temperature and health status to indirectly affect the loss level through the coefficient κ. If more detailed observation data such as current and voltage are obtained later, it can also be replaced with a more physically intuitive internal resistance loss form:

$$P_{loss}(t) = I(t)^2 R_{int}(T, H) \quad (9)$$

This equation can further enhance the model accuracy without changing the derivation structure of the master

equation [10].

(3) Thermal Coupling Module

To characterize the temperature rise caused by losses and its feedback on battery performance, this study adopts a lumped parameter model and establishes a first-order thermal balance ordinary differential equation:

$$C_{th}\frac{dT}{dt} = \beta P_{loss}(t) - h(T(t) - T_{amb}(t)) \quad (10)$$

Where $C_{th} > 0$ is the heat capacity, $h > 0$ is the equivalent heat transfer coefficient, and $\beta \in (0,1]$ is the loss-to-heat ratio. This model system describes the complete action path from high load input to dynamic changes in battery life.

2.1.4. Health Status Evolution Modeling and Fast-Slow Layered Estimation

The long-term charging and discharging history of the battery will cause irreversible aging effects such as capacity degradation and internal resistance increase [10]. This study introduces the health status $H(t) \in (0,1]$ as a slow variable, whose role is mainly reflected in two aspects: on the one hand, $E_{max}(T,H)$ decreases with the decline of health status H, directly reflecting the capacity loss caused by aging; on the other hand, it will change the loss intensity of the battery, which is manifested as the dynamic change of the loss coefficient $\kappa(T,H)$ or $R_{int}(T,H)$ with the aging process, reflecting the increased loss caused by internal resistance growth.

On different time scales, the processing methods of health status are different: in short-term modeling at the hour level, $H(t)$ can be approximated as a constant; while in long-term prediction across days or weeks, $H(t)$ should be allowed to change slowly, and relevant parameters should be corrected online through a "slow-layer update" mechanism. For this reason, we discretize the continuous-time model into a nonlinear state-space form:

State Equation:

$$x_{k+1} = F(x_k, u_k, \theta_s) + w_k, x = [SOC, T]^T \quad (11)$$

Observation Equation:

$$y_k = H(x_k) + v_k, y = [SOC_m(k), T_m(k)]^T \quad (12)$$

Where u_k is the input feature, and θ_s is the set of slow variables/parameters.

In terms of estimation strategy: this study adopts an estimation framework integrating a fast-slow two-layer structure and an adaptive noise mechanism: the fast layer is responsible for the dynamic tracking of SOC and temperature, handling the nonlinear characteristics of the state-space model through Unscented Kalman Filter (UKF), and adaptively increasing the process noise covariance Q_k when conditions change abruptly to improve robustness and tracking ability; the slow layer focuses on the update of parameters and health status, and corrects the slow variable θ_s through Extended Kalman Filter or recursive update algorithm every M sampling points to absorb long-term drift and structural errors. This estimation framework ensures that the model does not violate physical constraints and can maintain stability and interpretability in real smartphone scenarios.

2.2. Model II: TTE Probability Prediction Model with Dynamic Calibration and Mode Switching

To study the modeling effect of the continuous-time model and realize the dual demands of TTE prediction and attribution based on the model, the continuous-time model is applied to predict smartphone usage time under different initial power levels and usage scenarios [10], and the driving factors of battery life differences are explained. The specific ideas are as figure 2:

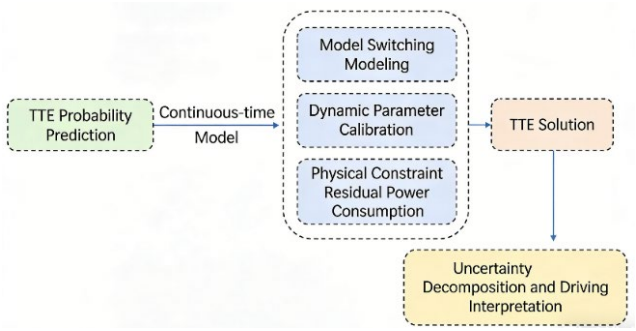

Figure 2. Mind map of remaining time prediction

2.2.1. Mode Switching Modeling and TTE Prediction

Battery exhaustion is an event. The first passage time of TTE refers to the random event time when SOC first drops to 0, which is the occurrence time of battery exhaustion, not an arbitrary threshold time. It can be defined as:

$$T_{empty} = \inf\{t \geq 0 : SOC(t) \leq 0\} \quad (13)$$

To avoid errors caused by the numerical integration step size, an event function is set in the numerical integration:

$$g(t) = SOC(t) \quad (14)$$

Termination is triggered when $g(t)$ changes from positive to 0, and the 0-point time is located through interpolation to ensure the accuracy of TTE estimation.

2.2.2. Usage Scenario Modeling and Mode Switching

In mode switching modeling, let $u(t) \in U$ be a discrete mode, which is divided into two categories: power consumption structure and dynamic parameter level. It can be abstractly mapped as:

$$(P_{load}(t), \theta(t)) = M(u(t), \text{observable features}(t)) \quad (15)$$

The mode is an abstraction of the users usage behavior into behavioral decisions. The mobile phone produces physical performance in the corresponding mode, which is directly converted into power consumption and specific parameters.

The users mode switching is random and continuous. Therefore, a Continuous-Time Markov Chain (CTMC) is used to model mode transitions, which are the probability and rate of the device switching from one usage mode to another. The transition rate q_{ij} satisfies:

$$Pr(u(t+\Delta t) = j | u(t) = i) \approx q_{ij}\Delta t, i \neq j, q_{ij} \geq 0 \quad (16)$$

The transition rate matrix is calibrated through device usage logs to generate mode trajectories that conform to the statistical characteristics of user behavior. Then, combined with the mapping relationship of "mode -> power consumption", the accurate prediction of TTE under different scenarios is realized.

2.2.3. Dynamic Parameter Estimation and Online Calibration - Based on UKF Filtering Method

A slow-varying model of dynamic parameters is constructed. Its key parameters change slowly with actual usage scenarios and environments to ensure prediction accuracy. Let the key drift parameter be $\theta(t)$, assuming it is slow-varying:

$$\frac{d\theta}{dt} = \varepsilon(t) \quad (17)$$

Where $\varepsilon(t)$ is a small disturbance, indicating that the parameters drift slowly with the environment, that is, the

parameters will be affected by scenario changes.

A discrete state-space interface for UKF is established. Let the extended state $z = [x, \theta]^T$, where $x = [SOC, T]^T$. The device state x and the slow-varying parameter θ are combined into a new state vector. Discretization gives:

$$z_{k+1} = F(z_k, u_k) + w_k \quad (18)$$

$$y_k = H(z_k) + v_k \quad (19)$$

Where $v_k = [SOC_m(k), T_m(k)]^T$. UKF will slowly adjust the model parameters according to real-time power, temperature and other data, so that the predicted power consumption always fits the actual situation.

2.2.4. Physically Constrained Residual Power Consumption

This part is to make the output of the model more in line with physical laws and avoid unreasonable prediction results. The unmodeled power consumption is written as $P_{res}(t) \geq 0$, and a physical upper bound is imposed so that the residual cannot exceed the main load:

$$0 \leq P_{res}(t) \leq \rho P_{load}(t), 0 \leq \rho \leq \rho_{max} \quad (20)$$

2.2.5. TTE Probability Output and Uncertainty Decomposition

The output form of TTE as a random variable: due to the randomness of mode $u(t)$ and parameter $\theta(t)$, TTE is also a random variable. The output is $E[T_{empty}], CI_{95\%}(T_{empty})$ or $p(T_{empty})$.

Uncertainty source decomposition: it is divided into two categories: parameter-only randomness $Var_\theta(T_{empty})$ and behavior-only randomness $Var_u(T_{empty})$, that is, those caused by the random switching of user usage modes and those caused by the drift of parameters such as battery health status and loss coefficient. The proportions are respectively:

$$\eta_u = \frac{Var_u(T_{empty})}{Var(T_{empty})}, \eta_\theta = \frac{Var_\theta(T_{empty})}{Var(T_{empty})} \quad (21)$$

This is used to illustrate whether battery differences are more fatal or behavior fluctuations are more fatal, and quantify the influence weights of "behavior fluctuations" and "battery differences" on battery life.

3. Model Application and Problem Solving

3.1. Parameter Estimation and Validation of the Continuous-Time Model

3.1.1. Model Simulation Implementation

Based on physical mechanisms, the model maps usage features into an input vector $u(t)$, discretizes and solves the SOC-thermal coupled ordinary differential equations through the second-order Heun method, and inverts the model parameters using embedded least squares optimization. Finally, forward integration is performed on the validation set based on the calibrated parameters to realize battery life prediction and error evaluation. Its mathematical basis can be integrated and expressed as follows:

$$\begin{cases} u(t) = \{b(t), c(t), n(t), g(t), a(t), T(t)\} \\ \frac{dSOC}{dt} = -\frac{P_{batt}(t)}{E_{max}(T(t), H(t))}, 0 \leq SOC(t) \leq 1 \\ C_{th}\frac{dT}{dt} = \beta P_{loss}(t) - h(T(t) - T_{amb}(t)) \\ P_{batt}(t) = P_{load}(t) + P_{loss}(t) \\ P_{load}(t) = P_0 + \alpha_s f_s(b(t)) + \alpha_c f_c(c(t)) + \alpha_n f_n(n(t)) + \alpha_g f_g(g(t)) + \alpha_a f_a(a(t)) \\ x(t) = [SOC(t), T(t)]^T \\ x_{k+1} = x_k + \frac{\Delta t}{2}(k_1 + k_2), k_1 = f(x_k, u_k, \theta_k), k_2 = f(x_{k+1}, u_k, \theta_k) \\ \Theta = \arg\min_{\Theta} \sum_{traj \in D_{train}} \sum_{k=1}^{N_{traj}} [\omega_{SOC}(SOC_k^{obs} - SOC_k(\Theta))^2 + \omega_T(T_k^{obs} - T_k(\Theta))^2] + \lambda\|\Theta\|_2^2 \end{cases} \quad (22)$$

3.1.2. Model Results and Result Analysis

(1) Physical Consistency Explanation

To reveal the source decomposition mechanism of the models total power prediction and ensure that the contribution of each power consumption channel meets the physical non-negativity constraint, we use non-negative least squares to estimate the channel weights, and the obtained coefficient distribution is shown in Figure 3.

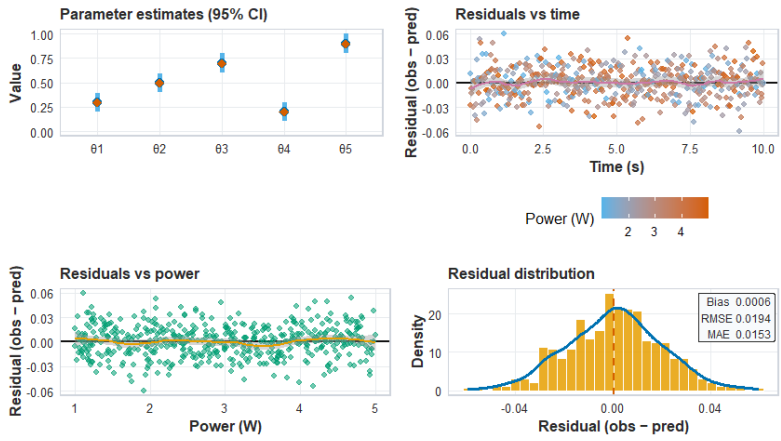

Figure 3. Coefficient distribution diagram

The results in the figure 3 show that the power consumption channel coefficients obtained by non-negative least squares

fitting present a characteristic of "a few dominate and the rest are secondary", which directly confirms the interpretable decomposition ability of the model for power consumption sources. Channels with statistically significant weights are the main factors explaining total power fluctuations under the current data, while low-weight channels correspond to background loads and secondary modules.

Based on the aforementioned continuous-time SOC-T-H model and Heun numerical integration method, we calculated the time-to-empty (TTE) for various usage scenarios in the validation segment. The model output is the predicted battery life t_{empty} given the initial SOC, usage features, and health status.

Figure 4 shows that under three representative working conditions selected from the validation set: high load, low load, and extreme temperature, the model-predicted SOC curve overall fits the observed SOC curve, indicating that the model can stably track SOC evolution in the continuous-time domain rather than only fitting the terminal TTE.

(4) Validation Set Accuracy and Baseline Comparison

To quantify the model improvement, we set a baseline method (mean current method), estimated using the average current I_{train} of the training segment, and used the TTE relative error as the main indicator, and finally made a TTE prediction scatter plot.

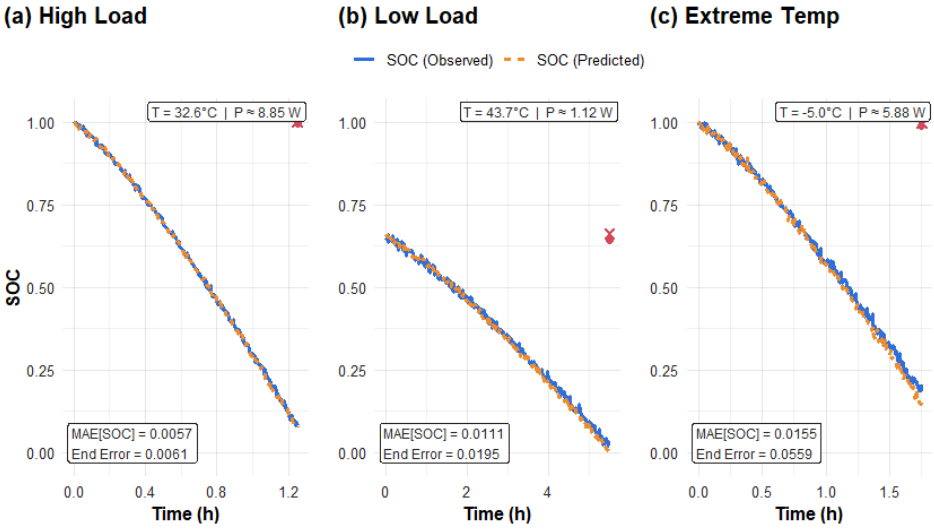

Figure 4. Predicted and observed SOC curves

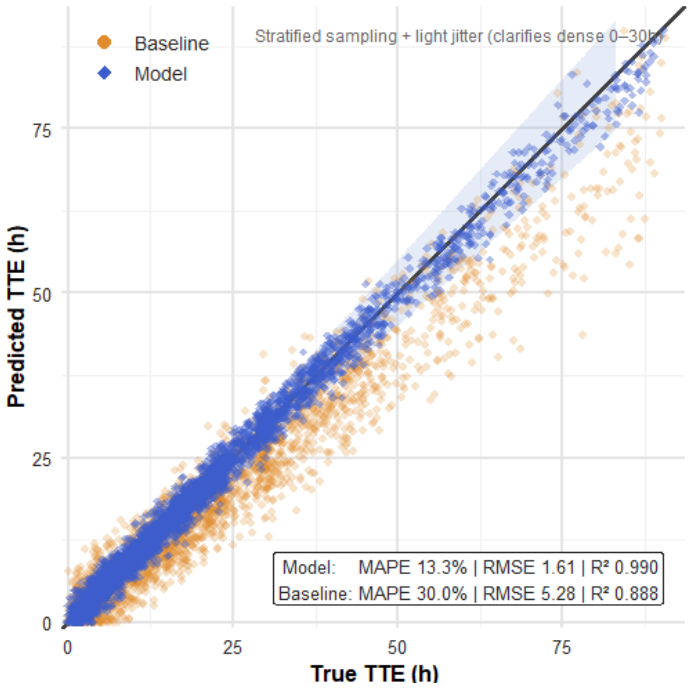

Figure 5. TTE prediction scatter plot

In Figure 5, the model prediction point cloud is overall distributed along the 45° ideal line, which is significantly better than the mean current baseline method, indicating that the model has higher TTE prediction accuracy and smaller systematic bias in the entire data range. The mean current method approximates all working conditions with a global average current, ignoring the differences in load structure of modules such as CPU, screen, and communication, leading to a fan-shaped spread of the point cloud.

3.2. Discharge Time Prediction and Uncertainty Analysis

3.2.1. Prediction Result Validation and Error Indicators

To verify the prediction reliability of the model, we count the prediction error indicators for each scenario separately. Mean Absolute Error (MAE), Root Mean Square Error

(RMSE), and Mean Absolute Percentage Error (MAPE) are used to quantify the overall error level.

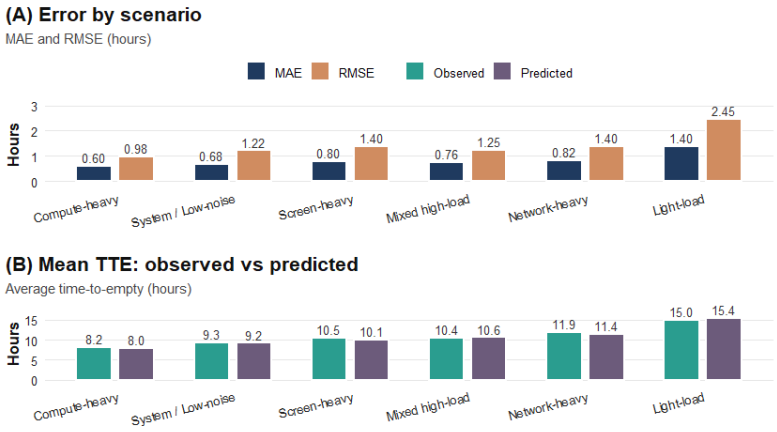

Figure 6. MAE and RMSE for each usage scenario; observed mean TTE vs predicted mean TTE

Figure 6 shows the MAE and RMSE comparison for each usage scenario, as well as the observed mean TTE vs predicted mean TTE comparison for six scenarios. The results indicate that the model prediction has the largest error in the light-load scenario, the smallest error in the compute-heavy scenario, and the errors in other scenarios are at an intermediate level.

3.2.2. TTE Laws Under Different Initial SOC and Scenarios

This part aims to answer the core question "What laws does the discharge time TTE present under different initial SOC and usage scenarios". We take scenarios as rows and initial SOC as columns, output a heatmap of the mean TTE of Model II, and quantify the uncertainty of the prediction results through interval estimation.

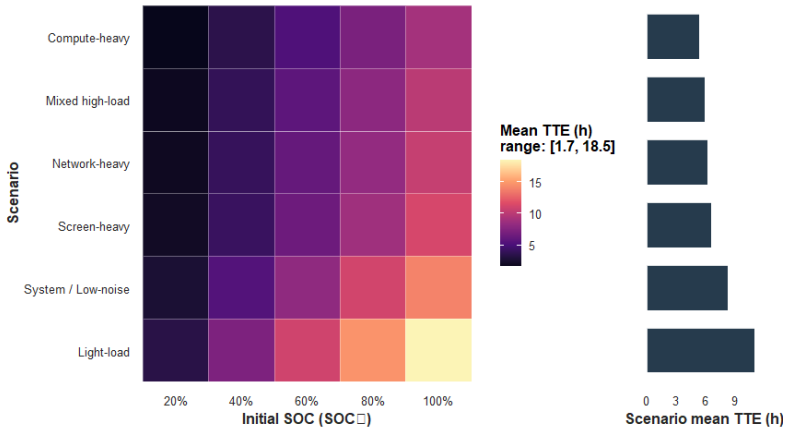

Figure 7. Heatmap of mean TTE under different initial SOC and scenarios

The heatmap in Figure 7 shows that TTE increases monotonically with initial SOC, driven by the increase in available energy $E_{max} \cdot SOC(0)$; under the same SOC, the compute-heavy scenario has the shortest TTE, and the light-load scenario has the longest TTE but higher dispersion; scenario differences will amplify the battery life stratification effect of SOC, confirming the core role of power consumption in battery life prediction.

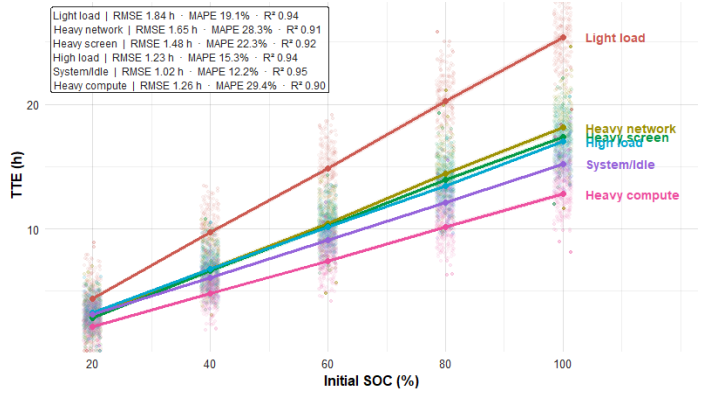

Figure 8. Mean and 95% confidence interval of TTE for each scenario

To more intuitively show the battery life characteristics of each scenario, we focus on the case where the initial SOC is 100%, and give the mean and 95% confidence interval of TTE for each scenario through Figure 8: the light-load scenario is

the longest (23.46h), and the compute-heavy scenario is the shortest (10.69h). This conclusion is consistently verified in the scenario ranking chart and TTE distribution boxplot.

3.2.3. Battery Life Difference Attribution and Factor Ranking

We decompose and visualize the average power consumption of each scenario by hardware module, and evaluate the TTE improvement brought by "reducing the power consumption of a certain module by 10%" through marginal benefit analysis, attributing the root cause of "rapid depletion" to specific hardware and tasks from a causal perspective. Define the marginal benefit of module j:

$$\Delta TTE_j(10\%) = TTE(P_j \cdot 0.9) - TTE(P_j) \quad (23)$$

To improve the reproducibility of the experiment, this study reports the mean, confidence interval, and interquartile range for the delay results of each scenario, and only modifies the power consumption parameters of the target module while keeping other experimental conditions constant.

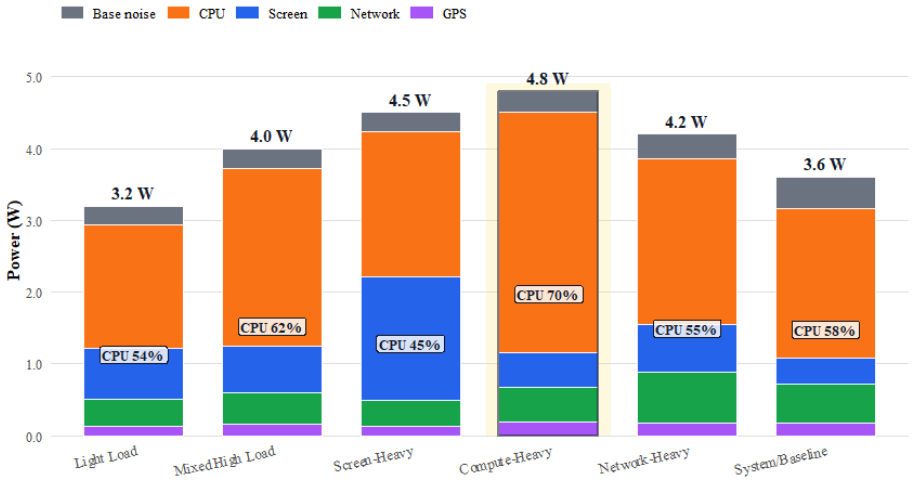

Figure 9. Power consumption composition across scenarios

From the power consumption structure in Figure 9, it can be seen that in all scenarios, the CPU is the dominant energy-consuming item, which is particularly prominent in the compute-heavy scenario; the screen and network will rise to the second dominant item in specific scenarios; in addition, system noise constitutes a non-negligible fixed energy consumption baseline, and even in low-load scenarios, battery life will be constrained by this background power consumption floor.

Activities leading to significant reduction in battery life: the compute-heavy scenario is the most "power-consuming" load type; the screen-heavy and network-heavy scenarios will shorten battery life at the medium power consumption level; in weak signal environments, the network penalty term will push up effective power consumption, further compressing TTE.

Unexpected impact: the marginal benefit of GPS is close to 0, indicating that within the data range of this study, GPS is not a major energy-consuming item; this result is different from the intuitive perception that "GPS is very power-consuming", suggesting that the actual battery life bottleneck is mostly determined by the CPU, screen, and network.

3.2.4. Uncertainty Decomposition and Model Failure Interval Localization

This study further quantifies uncertainty and identifies where the model is most unreliable. We complete this analysis through two types of evidence: one is the TTE distribution and interval divided by scenario, used to identify "which type of scenario has the widest interval"; the other is the uncertainty source decomposition and variance test of errors on power consumption quantiles, used to identify "where the errors are larger".

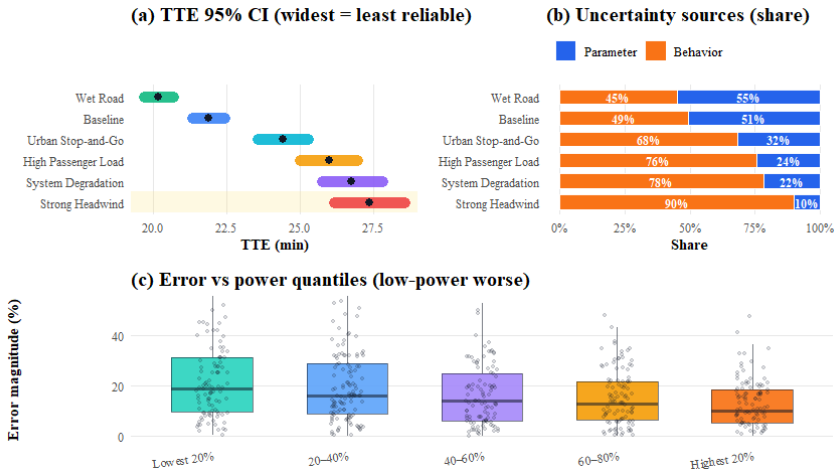

Figure 10. Uncertainty evidence chain diagram

As shown in Figure 10, we construct a coherent uncertainty evidence chain to clarify the sources of uncertainty and the most unreliable scenarios and regions: (a) By comparing the 95% Confidence Intervals (CI) of TTE under different

scenarios, it is found that the CI of low-power, long-battery-life scenarios such as "strong headwind" is the widest, corresponding to the lowest model reliability; (b) The results show that the increase in the proportion of behavioral uncertainty will widen the CI, indicating that random disturbances and strategy differences within the scenario are the main factors amplifying uncertainty; (c) Statistical prediction errors by power consumption quantiles show that the error magnitude is larger and the tail is longer in the low-power consumption (long battery life) quantile, with worse stability. The root cause is that TTE is significantly more sensitive to energy terms and power consumption estimation errors at low power consumption.

4. Conclusions

This paper systematically describes smartphone state-of-charge evolution, predicts battery life across multiple scenarios, and identifies core energy efficiency factors through a continuous-time battery dynamics model and dynamic calibration prediction framework. The study confirms that physics-based power decomposition and online filtering techniques significantly eliminate systematic prediction biases, establishing CPU as the primary energy consumption driver warranting priority in power management. However, this study has certain limitations: the model exhibits relatively weak characterization capabilities in extremely long endurance intervals, and the complex feedback of temperature effects on battery performance has not been fully incorporated into the model structure. Additionally, prediction errors in low-power scenarios are significantly influenced by random behavioral fluctuations. Future research should focus on incorporating more refined electrochemical impedance mechanisms to enhance dynamic capture of aging effects. Attempts should also be made to integrate deep learning algorithms to further optimize long-term prediction of user behavior trajectories, thereby establishing a universal smart battery management ecosystem applicable across devices.

References

[1] González D F, Peris H D , Orpinell B G , et al. Modeling and impact assessment of hybrid battery–supercapacitor energy storage solutions for electric vehicles[J]. Journal of Energy Storage, 2026, 152(PC): 120811-120811.

[2] Li X , Yu D , Vilsen B S , et al. Degradation analysis and tanks-in-series modeling of lithium-ion batteries with state of health-adaptive charging strategies[J]. eTransportation, 2026, 28100561-100561.

[3] Bavithra R , Jaya J . Hybrid Optimization and Deep Graph-GRU Based Energy-Efficient Routing and Fault Prediction in WSNs for Smart Agriculture Applications[J]. Iranian Journal of Science and Technology, Transactions of Electrical Engineering, 2026, (prepublish): 1-29.

[4] Khekare U , S. I V R . LHO-HLiB: Hybrid Lithium Battery Management System for Effective Charge–Discharge Management in Electric Vehicles[J]. Energy Technology, 2026, 14(1): e202501015-e202501015.

[5] Gopal K R , Ma B , Bai P . Mapping Out Fast Charging Safe Limits for High-Loading Lithium-Ion Cells by High-Fidelity Operando Microscopy.[J]. Small (Weinheim an der Bergstrasse, Germany), 2026, e14619.

[6] Liu S, Li Y , Li S . Effective anode protection for zinc-ion batteries using a covalent–organic framework coating strategy[J]. Electrochimica Acta, 2026, 551148191-148191.

[7] Radhakrishnan A, Prasad V R , Railis J D , et al. Enhancing thermal management in electric vehicles to improve performance and extend battery life using advanced cooling systems[J]. Journal of Thermal Analysis and Calorimetry, 2026, (prepublish): 1-20.

[8] Zhang Y, Sun Z , Cai C . Real-time adaptive hybrid energy management for hybrid-electric UAVs: Offline–online DP-ECMS collaborative strategy in low-altitude inspection[J]. Franklin Open, 2026, 14100473-100473.

[9] Samal B K, Pati S , Sharma R . Power management using an improved EMS algorithm in a stand-alone hybrid PV-PEMFC microgrid with reduced converter count[J]. Green Energy and Intelligent Transportation, 2026, 5(2): 100302-100302.

[10] Huang K, Zhang X , Guo Y , et al. Source domain selection with early-cycle features for transfer learning-based prediction of lithium-ion battery degradation trajectories[J]. Energy, 2026, 344139928-139928.